Solid State Ionics 444 (2026) 117265

Contents lists available at ScienceDirect

Solid State Ionics

journal homepage: www.elsevier.com/locate/ssi

Benchmarking the electronic transport properties of lithium thiophosphate glasses and glass-ceramics using double-blocking-electrode polarization

Ratnottam Das [a], Ruihao Deng [a], Sara Seelman [b], Keng Xu [a], Alisha Toporski [a], Ru Xiao [a], Ruixin Wu [a], Fudong Han [a,b,*]

[a] *Department of Mechanical, Aerospace and Nuclear Engineering, Rensselaer Polytechnic Institute, Troy, NY 12180, United States*
[b] *Department of Materials Science and Engineering, Rensselaer Polytechnic Institute, Troy, NY 12180, United States*

ARTICLE INFO

Keywords:
Solid-state batteries
Electronic transport
Diffusion
Minority carriers
Solid electrolytes
Activation energy
Double-blocking-electrode polarization

ABSTRACT

The partial electronic conductivity (σ_{el}) in Li solid electrolytes (SEs) has important implications in determining the self-discharge rate and degradation processes of solid-state batteries, but reliable scientific data on the electronic transport properties of Li SEs remain scarce. While Hebb-Wagner polarization measurement using asymmetric cells with a single ionic-blocking electrode has been reported as a powerful technique to probe σ_{el} at different Li activities, we suggest that it is not suitable for probing the intrinsic electronic transport properties of lithium thiophosphate-based SEs due to unavoidable anodic decomposition of the SE. Polarization using double-blocking-electrode cells is, therefore, proposed as a more appropriate technique to determine the σ_{el} at a specific Li activity related to the Li activity of the unpolarized SE. Using temperature-dependent double-blocking-electrode polarization, we examine the electronic transport properties of common lithium thiophosphate glass and glass-ceramic SEs, including Li_3PS_4 and $Li_7P_3S_{11}$ glasses; Li_3PS_4 and $Li_7P_3S_{11}$ glass-ceramics with varying crystallinity, as well as Cl-doped and N-doped Li_3PS_4 glasses with varying dopant concentrations. The results provide a reliable basis to investigate the effect of annealing and doping conditions on the electronic transport properties. Among all conditions, N^{3-} doping was found to exhibit the largest effect on increasing σ_{el}. Moreover, all SEs studied in this work exhibit two distinct linear regimes in the Arrhenius plots of σ_{el}: a low-temperature regime with a lower activation energy, and a high-temperature regime with a higher activation energy. These findings provide important insights into understanding the electronic transport and conduction mechanisms in lithium thiophosphate-based SEs.

1. Introduction

An ideal solid electrolyte (SE) should have a high ionic conductivity (σ_{ion}) but a low electronic conductivity (σ_{el}) [1–3]. While significant efforts have been devoted to understanding and improving the ionic transport properties of Li SEs with many materials, such as Li_2S-P_2S_5 [4–6], Li_6PS_5Cl [7], and $Li_{10}GeP_2S_{12}$ [8], exhibiting a similar or even higher σ_{ion} when compared with liquid electrolytes, the electronic transport in these SEs has rarely been studied, probably because the reported σ_{el} of most Li SEs are orders of magnitude lower than the corresponding ionic conductivities. It has therefore been taken for granted that such a small electronic conduction is negligible. However, even very small σ_{el} can lead to perceptible self-discharge, especially when the battery is not under constant use [9]. A recent study by Deng et al [10] showed that reversible capacity loss due to electronic leakage can dominate capacity decay over irreversible losses during calendar aging of Li_6PS_5Cl-based solid-state batteries, leading to a short calendar life of <3 years at room temperature. The residual σ_{el} of Li SEs was also reported to accelerate the electrochemical decomposition of solid electrolytes [11–13], as well as promote the internal deposition of Li dendrites in SEs [14–16]. Therefore, there is a pressing need to investigate the electronic transport and conduction mechanisms in Li SEs to develop strategies to lower σ_{el} in SEs for the development of high-performance solid-state batteries [17,18].

Understanding electronic transport in SEs first requires accurate and reliable σ_{el} measurements, which have proven challenging. Significant variations in the measured electronic conductivities can be observed for SEs with the same SE [9]. The electronic conductivity of Li SEs was usually measured by DC polarization of two different ionic-blocking cells: (i) Hebb-Wagner cells with one reversible electrode (RE) and

---

* Corresponding author at: Department of Mechanical, Aerospace and Nuclear Engineering, Rensselaer Polytechnic Institute, Troy, NY 12180, United States.
E-mail address: hanf2@rpi.edu (F. Han).

https://doi.org/10.1016/j.ssi.2026.117265
Received 31 March 2026; Received in revised form 16 May 2026; Accepted 24 June 2026
0167-2738/© 2026 Elsevier B.V. All rights are reserved, including those for text and data mining, AI training, and similar technologies.

one blocking electrode (BE) [19–22] (Fig. 1a), and (ii) double-blocking-electrode cells with two BEs (Fig. 1b) [1,23,24]. Initial polarization of these cells leads to migration of all charge carriers. Since the ionic transport is blocked, however, at steady state only electronic carriers (electrons and holes) are allowed to move. Given that the concentration of ionic defects is high and the concentrations of electronic carriers are small, the chemical potential gradient of the ions can be neglected. The high concentration of ionic defects also does not permit the build-up of an electric field, since any potential difference across the SE can be compensated by the redistribution of ionic carriers. As a result, the transport of electronic carriers is driven solely by its concentration gradient, following Fick's law [25]. Assuming that steady state conduction is determined by just one electronic carrier (electron or hole), the evolution of the concentration profiles of the electronic carrier during DC polarization can be determined for Hebb-Wagner cells (Fig. 1c) and double-blocking-electrode cells (Fig. 1d) [24]. A four times longer period is needed for Hebb-Wagner cells to reach steady state under a fixed polarization voltage (i.e., fixed range of Li activity/concentration) across the cell [23].

The concentration gradient of electronic carriers in the SE also suggests that the σ_{el} varies with position (x), as it depends on the local lithium activity, which is inherently linked to the potential of each electrode. As a result, Hebb–Wagner method should be, in principle, a preferred method for determining the Li activity-dependent electronic conductivity by fixing the electrode potential (i.e., Li activity) at the RE. By adjusting the potential of the BE, the σ_{el}, including both electron conductivity (σ_e) and hole conductivity (σ_h), at the lithium activity of the BE electrode can be determined by

$$\sigma_{el}[a_{Li}(\mathrm{BE})] = \sigma_{e+h}[a_{Li}(\mathrm{BE})] = -L\frac{dj_{el,ss}}{dU} \tag{1}$$

where $j_{el,ss}$ is the steady state current density measured at each polarization voltage U. The electron conductivity (σ_e) and hole conductivity (σ_h) at the lithium activity of the RE can also be separately determined from the slope and the axial intersection of the plot of $\left|j_{el,ss}\right| / \left(\exp\left(\frac{\alpha FU}{RT}\right) - 1\right)$ versus $\exp\left(-\frac{\alpha FU}{RT}\right)$ based on

$$\left|j_{el,ss}\right| \Big/ \left(\exp\left(\frac{\alpha FU}{RT}\right) - 1\right) = \frac{RT}{\alpha FL}\left(\sigma_e \exp\left(-\frac{\alpha FU}{RT}\right) + \sigma_h\right) \tag{2}$$

where T is absolute temperature, R is the ideal gas constant, F is the Faraday constant and α is a characteristic exponent derived from the defect chemistry based on

$$\frac{\mathrm{dln}\sigma_{el}}{\mathrm{dln}a_{Li}} = \alpha \tag{3}$$

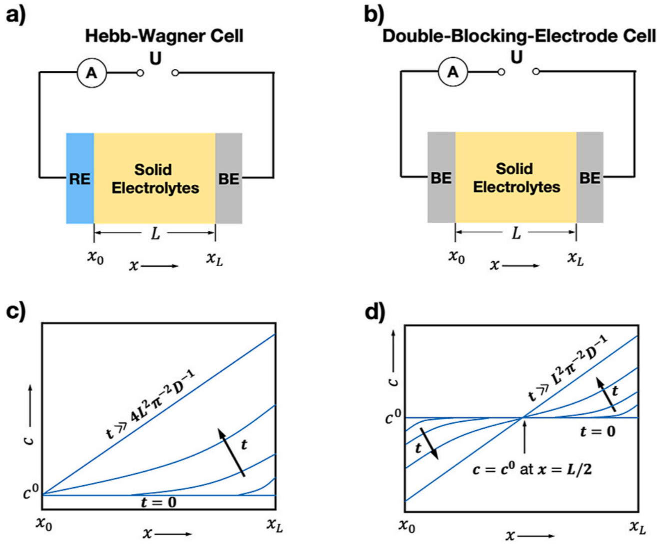

Fig. 1. Schematic showing a Hebb-Wagner cell (a) and a double-blocking-electrode cell (b). Schematic showing the development of the linear stationary concentration of the electronic carrier during DC polarization in a Hebb-Wagner Cell (c) and in a double-blocking-electrode cell (d) assuming just one charge carrier (electron or hole) determines the steady state conductance (t, time constant; L, sample thickness; D, diffusion coefficient).

Despite the informative results from the Hebb-Wagner method, implementation of measurements can be quite challenging because of the limited electrochemical stability of lithium thiophosphate-based solid electrolyte (~1.7 to ~2.1 V vs. Li/Li$^+$) [26–29]. The electrochemical reduction/oxidation of the SE leads to an inaccurate determination of Li activity at each electrode [30–32]. More importantly, the oxidation of the SE at the BE essentially makes the Hebb-Wagner cell a battery that introduces ionic currents at the "steady state" [9], leading to overestimated currents. Because the steady state current from electronic transport is typically very small for most solid electrolytes, even a slight oxidation of the SE can lead to a significant overestimate in the measured electronic conductivity. The limited electrochemical stability of lithium thiophosphate-based solid electrolyte introduces an inherent challenge to find an RE that is electrochemically stable with the solid electrolyte. Even if one can find an RE with an electrode potential of >1.7 V vs. Li/Li$^+$, the voltage range (or correspondingly Li activity range) that can be probed for the BE is limited to <2.1 V (corresponding to a cell voltage of 0.4 V). Moreover, due to possible surface oxidation of the SE, the open circuit voltage (OCV) of the SE on the BE side can be much higher than its theoretical electrode potential. The OCV of an as-fabricated $Li_{0.5}In/Li_3PS_4/SS$ cells is around 1.8 V (Fig. S1), indicating that electrode potential on the BE side is 2.4 V vs. Li/Li$^+$, which is already higher than the anodic limit of the SE, preventing any possible measurements without the decomposition of the SE. We believe this is also the reason why the reported electronic conductivity of Li_6PS_5Cl SEs from Hebb-Wagner measurement is one or two orders of magnitude higher than the value estimated from the reversible capacity loss of a full cell during calendar decay [9,12]. To address this challenge, a modified Hebb-Wagner method based on two-step polarization, consisting of a high voltage polarization (at 4.4 V vs. Li/Li$^+$) to decompose the SE as much as possible followed by a low voltage polarization (at 4.2 V vs. Li/Li$^+$), was proposed by Shao et al [9] to determine the overall σ_{el} of thiophosphate-based SE and its decomposed interphases. While the information can help reflect the σ_{el} of the thiophosphate-based SE in a high-voltage solid-state cell because the SE will decompose anyway in a high-voltage cell, it cannot separate the contribution of σ_{el} from the SE and that of the decomposed interphases, and therefore cannot be used to probe the electronic transport properties of the SE itself.

It is therefore proposed that double-blocking-electrode cell measurement should be used as a more reasonable approach to determine the intrinsic electronic transport properties of thiophosphate-based SEs. A few reasons were reported to explain why the σ_{el} measured from DC polarization of double-blocking-electrode cells is not reliable. Firstly, only an average σ_{el} can be determined from the double-blocking-electrode cells based on Ohm's law, but Ohm's law does not hold true anymore for diffusion-driven transport of electronic carriers [33]. Secondly, since both BE do not possess a defined lithium activity, it is unclear at what lithium activity the electronic conductivity of the SE was measured [9,33]. Nevertheless, the theory of electronic conductivity in an activity gradient has been well studied by Maier [24]. Based on the diffusion of electronic carriers in an Li activity gradient, the voltage-current relation from a double-blocking-electrode polarization should follow

$$\frac{U}{j_{el,ss}} = \int_{x_0}^{x_L} \frac{dx}{\sigma_{el}(x)} \tag{4}$$

where $x_0 = 0$ and $x_L = L$ in Fig. 1b, and $\sigma_{el}(x)$ is local electronic conductivity of SE at various x. Eq. 4 can be interpreted as a series of different resistors ($dR_{el} = dx/\sigma_{el}(x)$) each with a locally constant conductivity. Correlating Eq. 4 with Ohm's law ($U/j_{el,ss} \equiv L/\overline{\sigma_{el}}$), where $\overline{\sigma_{el}}$ is considered the average electronic conductivity,

$$\frac{U}{j_{el,ss}} \equiv \frac{L}{\overline{\sigma_{el}}} = R_{el} = \int_{x_0}^{x_L} dR_{el} \tag{5}$$

The average electronic conductivity $\overline{\sigma_{el}}$ and local electronic conductivity $\sigma_{el}(x)$ can then be linked by

$$\frac{L}{\overline{\sigma_{el}}} = \int_{x_0}^{x_L} \frac{dx}{\sigma_{el}(x)} \tag{6}$$

Assuming (i) just one carrier (electron or hole) dominates the σ_{el}, which is a reasonable assumption for measurements done in the limited range of lithium activity, and (ii) the polarization period is sufficiently long ($t \gg L^2\pi^{-2}D^{-1}$) so that a linear concentration profile of the electronic carrier is established (Fig. 1d), Eq. 6 can then be solved,

$$\overline{\sigma_{el}} = \frac{\sigma_{el}(x_0) - \sigma_{el}(x_L)}{\ln\sigma_{el}(x_0) - \ln\sigma_{el}(x_L)} \tag{7}$$

suggesting that the $\overline{\sigma_{el}}$ determined from double-blocking-electrode polarization is essentially linked to the σ_{el} at the lithium activity of each of the two BEs ($x_0 = 0$ and $x_L = L$ in Fig. 1b). Eq. 3 suggests that σ_{el} is proportional to $(a_{Li})^{\alpha}$, and one recognizes that the average electronic conductivity measured from double-blocking-electrode polarization equals the conductivity measured at a uniform lithium activity $\overline{a_{Li}}$, given by

$$(\overline{a_{Li}})^{\alpha} = \frac{(a_{Li}(x_L))^{\alpha} - (a_{Li}(x_0))^{\alpha}}{\ln(a_{Li}(x_L))^{\alpha} - \ln(a_{Li}(x_0))^{\alpha}} \tag{8}$$

Eq. 8 can be further exploited by considering the concentration profile of the electronic carriers in Fig. 1d. Because the boundary conditions at $x_0 = 0$ and $x_L = L$ are the same, the concentration profile is symmetric about the midpoint ($x_0 = L/2$), where the initial Li activity of the SE was maintained [24]. In other words, at the midpoint the concentration is maintained at the initial concentration c^0which is directly linked to the lithium activity in the unpolarized SE (a_{Li}^0). From Nernst equation, the lithium activity of the SE at $x_0 = 0$ can be obtained as

$$a_{Li}(x_0) = a_{Li}^0 \bullet \left(\frac{2}{\exp\left(\frac{\alpha FU}{RT}\right) + 1}\right)^{1/\alpha} \tag{9}$$

and the lithium activity of the SE at $x_L = L$ is

$$a_{Li}(x_L) = a_{Li}^0 \bullet \exp\left(\frac{\alpha FU}{RT}\right) \bullet \left(\frac{2}{\exp\left(\frac{\alpha FU}{RT}\right) + 1}\right)^{1/\alpha} \tag{10}$$

Substituting Eq. 9 and Eq. 10 into Eq. 8, one can get

$$\overline{a_{Li}} = a_{Li}^0 \bullet \left(\frac{2RT}{\alpha FU} \bullet \frac{\exp\left(\frac{\alpha FU}{RT}\right) - 1}{\exp\left(\frac{\alpha FU}{RT}\right) + 1}\right)^{1/\alpha} \tag{11}$$

As a result, the averaged electronic conductivity $\overline{\sigma_{el}}$ from the double-blocking-electrode cells can be considered as the σ_{el} at a uniform Li activity of $\overline{a_{Li}}$, which is directly related to the lithium activity of unpolarized SE (a_{Li}^0). Therefore, the averaged electronic conductivity $\overline{\sigma_{el}}$ can be used to compare the electronic conductivity of SEs with the same or similar compositions. In principle, since $\overline{a_{Li}}$ is also a function of cell voltage U (Eq. 11) it is also possible to measure the σ_{el} at different $\overline{a_{Li}}$ by changing U. However, $\overline{a_{Li}}/a_{Li}^0$ changes only by a factor of 0.13 as U increases from 0 to 0.4 V when $\alpha = 1$ (Fig. S2), while in a typical 4 V battery the Li activity within the SE changes by 34 or 68 orders of magnitude depending on the type of disorder. Therefore, not much information can be obtained by changing the polarization voltage with double-blocking-electrode cells. As a matter of fact, it is recommended that the polarization voltage be as small as possible, depending on the accuracy/resolution of current measurement, not only to prevent potential SE decomposition, but also, and more importantly, to limit the activity range between the two BEs so that only one minority carrier (electrons or holes) dominates electronic transport - a primary assumption in Maier's derivation [24]. The polarization period has to be sufficiently long ($t \gg L^2\pi^{-2}D^{-1}$) to ensure the establishment of a linear concentration profile (Fig. 1d) which is also used to derive Eq. 7. We believe the high polarization voltages (e.g., ≥0.5 V) [34–37] and the short polarization periods (e.g., ≤1 h) [4,14,34–37] are among the main reasons why previous double-blocking-electrode polarization measurements lead to unreliable results. Apparent deviations of the steady state current and the resultant electronic conductivity of Li_3PS_4 SE can be observed for the results measured by double-blocking-electrode polarization at voltages >0.5 V [9], due to the electrochemical decomposition of the SE. The decomposition of Li3PS4 can also be supported by the change of the Nyquist plots of the SS/LPS/SS cell from a blocking behavior to a non-blocking behavior as the polarization potential increases from 0.3 to 1.1 V (Fig. S3). While σ_{el} over a wide range of lithium activities cannot be probed with double-blocking-electrode cells, the measured $\overline{\sigma_{el}}$ does dictate the intrinsic electronic transport property of the SE itself without the effects of its electrochemical decomposition, which is a significant advantage over the Hebb-Wagner method.

In this work, we examine σ_{el} of lithium thiophosphate glass and glass-ceramic SEs using double-blocking-electrode DC polarization. In addition to a low polarization voltage of 0.3 V and a long polarization duration of 12 h, we also performed measurements at various temperatures, which have been rarely done in previous studies, to reveal the temperature-dependent electronic transport properties. We conservatively chose 0.3 V as the polarization voltage– high enough to allow us to reliably measure currents of up to picoampere range, and low enough to potentially prevent any electrochemical decomposition. Two representative lithium thiophosphate compositions were chosen: Li_3PS_4 (i.e., $75Li_2S\text{-}25P_2S_5$) and $Li_7P_3S_{11}$ (i.e., $70Li_2S\text{-}30P_2S_5$). Both systems are among the most widely studied lithium thiophosphate SEs and exhibit well-documented understandings of their ionic transport properties [38]. For Li_3PS_4, annealing-induced crystallization generally leads to a decrease in ionic conductivity [6,39–41], whereas for $Li_7P_3S_{11}$, the increase in crystallinity enhances ionic transport [42–44]. This opposing behavior provides a useful internal comparison framework for examining whether σ_e follows similar, inverse, or entirely decoupled trends relative to ionic transport. Beyond crystallinity, controlled doping was employed as a second lever to probe electronic transport [5,45]. Small concentrations of LiCl and Li_3N were selected as dopants for Li_3PS_4 glass to introduce lithium-poor ($Li_{3-4x}PS_{4-4x}Cl_{4x}$, x = 1, 3, and 5%) and lithium-rich ($Li_{3+4y}PS_{4-4y}N_{4y}$, y = 1, 3, and 5%) thiophosphates to understand their effects on electronic transport. These results provide a reliable basis for discussing electronic transport in lithium thiophosphate glass and glass-ceramic SEs and highlight the challenges and limitations that warrant further investigation.

2. Results and discussion

2.1. Temperature-dependent electronic conductivity measurement using DB cells

Double-blocking-electrode cells were fabricated by cold-pressing 150 mg of SE powder at 400 MPa between two stainless steel (SS) ion-blocking electrodes, which also served as current collectors. DC polarization was conducted at an applied potential of 0.3 V for 12 h at each measurement temperature. Fig. 2a shows the current-time curves of Li_3PS_4 glass SE measured at selected temperatures from room temperature to 100 °C. A longer duration is needed to polarize the cell at higher temperature, but the current variation for the last hour of the 100 °C measurement (red line) remains $<3\%$, suggesting that the duration is sufficient to reach a steady state. The steady state current was then used to determine the σ_{el} of the SE at various temperatures using Eq. 5. The electronic conductivity at room temperature is determined to be 0.9×10^{-10} S cm^{-1}. This value is about 1 order of magnitude lower than the reported result for Li_3PS_4 glass [9], suggesting that the proposed method can reduce the overestimate from the conventional approach with a larger polarization voltage or a shorter polarization duration. A typical Arrhenius plot of the resulting σ_{el} are presented in Fig. 2b. While a clear increase in σ_{el} with temperature can be observed, the plot clearly shows two distinct linear regimes: a low temperature regime with an activation energy of 0.26 eV, and a higher temperature regime with an activation energy of 0.52 eV. Such distinct regimes have not been shown, to the best of our knowledge, for Li solid electrolytes, but have been reported for electronic conduction in Na-β-alumina [46] and yttria-doped thoria [47]. While reliable reference values for E_a^{el} of Li SEs are scarce in literature, the E_a^{el} in the high-temperature regime is comparable with that of LiI (0.44 eV measured from 45 to 57.5 °C) [17]. Since the band gap of Li_3PS_4 is calculated to be 3.7 eV [48], the low activation energy for electronic conduction may be attributed to the localized states within the band gap, arising from native [49] or external [17] point defects and/or other types of disorder. The states can act as donors or acceptors, where electronic carriers are localized [50]. Electronic carrier hopping through these localized states can lead to significantly lower activation compared to the band gap. The distinct activation energy for electronic conduction suggests different hopping mechanisms involving localized states in the high-temperature and low-temperature regimes, although the exact sources of the localized states remain unknown.

In line with this observation, in the following study, we have reduced the number of temperatures for the measurements. Activation energies were extracted using linear fits over restricted temperature windows, corresponding to low- and high-temperature regimes and typically comprising three to four adjacent data points. The boundary separating the low- and high-temperature fitting regimes was not fixed a priori. This segmented fitting approach was adopted as a practical means of averaging experimental uncertainty while enabling internally consistent comparison across different samples. The extracted activation energies (E_a^{el}) are reported with the room-temperature σ_{el} for comparative analysis. In the next section, we first introduce the effect of individual annealing or doping conditions on the electronic conductivity and activation energy, followed by comparisons across different processing conditions and compositions. Nyquist plots of the SEs from EIS measurements are included (Figs. S4–S7) to understand the effect of processing and doping conditions on ionic transport. The current-time curves of the SEs during DC polarization of double-blocking-electrode cells are included in the supplementary materials (Figs. S8–S11). The values for the electronic and ionic conductivity of these SEs are tabulated in Tables S1–S4 in the supplementary materials.

2.2. *Effect of annealing on electronic transport of Li_3PS_4 glass and glass-ceramics*

We first investigated the effect of crystallinity on the electronic transport in Li_3PS_4 glass and glass-ceramic SEs. Li_3PS_4 glass-ceramics with various crystallinity were synthesized by annealing Li_3PS_4 glass (denoted as Li3-glass) at 200 °C for different durations from 5 min to 24 h (denoted as Li3-5 min, Li3-1 h, and Li3-24 h, respectively). The XRD of the Li3-glass exhibits broad features without distinct Bragg peaks (Fig. 3a), consistent with an amorphous structure. Upon annealing, the emergence of diffraction peaks is observed even after short annealing durations (5 min), indicating the onset of crystallization. The observed peaks can be indexed to the orthorhombic β-Li_3PS_4 phase (space group: *Pnma*) [39]. With increasing annealing duration, the intensities of these reflections increase, suggesting a progressive increase in the degree of crystallinity in the corresponding glass-ceramics. Raman spectra of Li_3PS_4 glass and glass-ceramic samples exhibit characteristic thiophosphate vibrational features, as shown in Fig. 3b. The spectra are dominated by a peak centered at ~425 cm^{-1}, commonly attributed to PS_4^{3-} tetrahedral units and a side peak at ~390 cm^{-1}, attributed to $P_2S_6^{4-}$ units. The peak corresponding to $P_2S_6^{4-}$ however disappears even on short annealing (5 min), consistent with the local structure evolution Li_3PS_4 upon crystallization [39]. The effect of crystallinity on the ionic transport properties also agrees with prior literature results (Fig. 3c and d) [39–41]. The Nyquist plots of Li_3PS_4 after annealing for various durations are included in Fig. S3. With increasing annealing duration, the ionic conductivity decreases from 0.36 to 0.07 mS cm^{-1}, with a slight increase in the activation energy (E_a^{ion}) from 0.34 to 0.35 eV (Fig. 3d).

Fig. 3e shows the Arrhenius plot of the electronic conductivity for Li-3 glass, Li3-5 min, Li3-1 h and Li3-24 h. All SEs show two linear regimes within the measured temperature range. The activation energy ranges from 0.40 to 0.52 eV in the high-temperature regime and 0.09 to 0.26 eV in the low-temperature regime. The room temperature electronic conductivity of Li_3PS_4 glass is 0.9×10^{-10} S cm^{-1}. A ~2× increase in the σ_{el} can be observed for Li3–5 min (Fig. 3f). Further increasing the annealing duration leads to slight increase but overall stabilized electronic conductivity of $\sim 1.9 - 2.0 \times 10^{-10}$ S cm^{-1} for Li3-1 h and Li3-24 h (Fig. 3f). Apparent drop of both high-temperature E_a^{el} from 0.52 to 0.40 eV and low-temperature E_a^{el} from 0.26 to 0.09 eV after annealing Li_3PS_4 glass for 5 min (Fig. 3g). The activation energies for both temperature regimes then increase and decrease with the annealing durations. Overall, in contrast with the effect of crystallinity on the ionic transport behavior, enhanced electronic transport is observed after annealing in

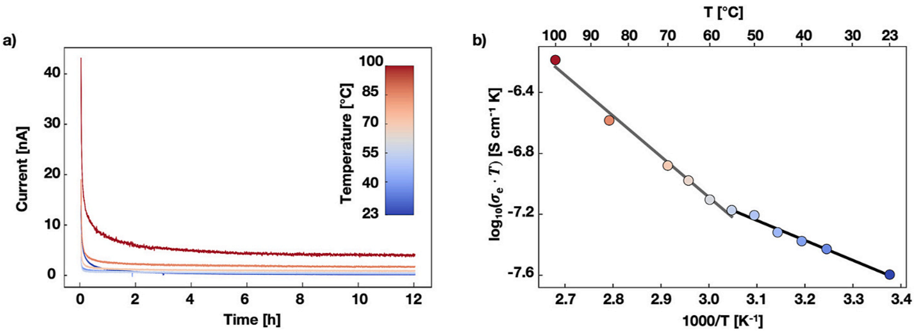

Fig. 2. a) Current-time curves of Li_3PS_4 glass at select temperatures measured by double-blocking-electrode cells. b) Arrhenius representation of σ_{el} for Li_3PS_4 glass in the temperature range of 23 to 100 °C.

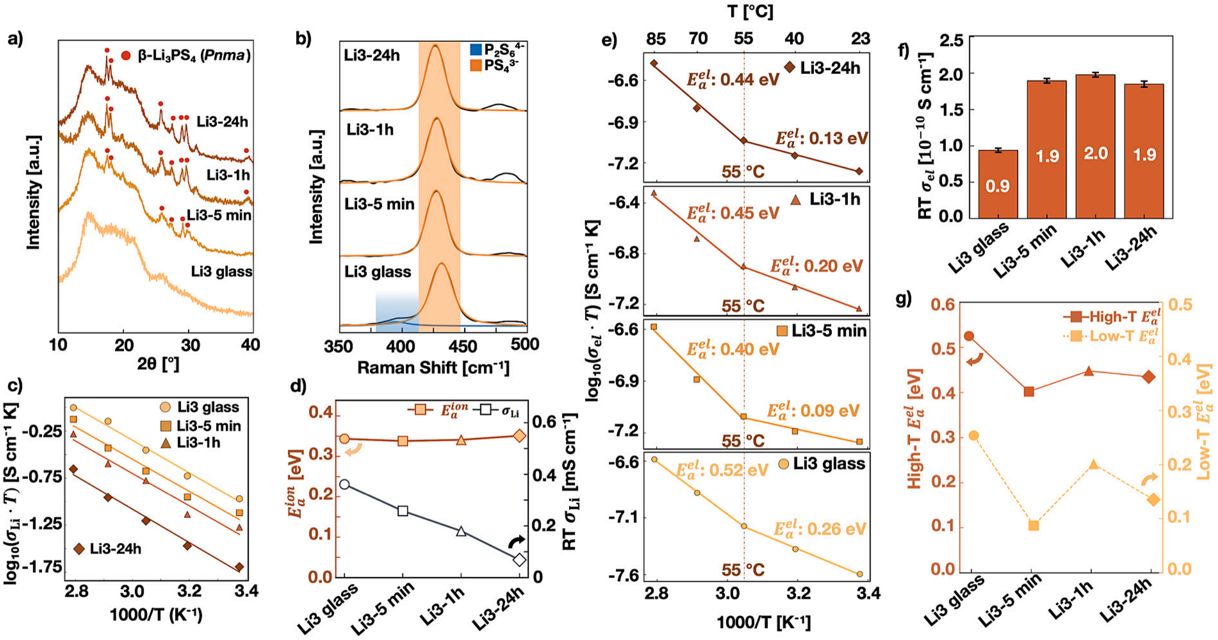

Fig. 3. Effect of annealing on the transport properties of Li_3PS_4 glass and glass-ceramics. X-ray diffraction (a), Raman spectra (b), Arrhenius plot of ionic conductivity (c), room temperature ionic conductivity and activation energy for ionic transport (d), Arrhenius plots of electronic conductivity (e), room temperature electronic conductivity (f), and activation energy for electronic transport (g) in Li_3PS_4 glass and glass-ceramics.

Li_3PS_4, with the most apparent enhancement observed after annealing for 5 min.

2.3. *Effect of annealing on electronic transport of $Li_7P_3S_{11}$ glass and glass ceramics*

We then studied the effects of crystallinity on the transport properties of $Li_7P_3S_{11}$ glass-ceramics. $Li_7P_3S_{11}$ glass-ceramics with various crystallinity were synthesized by annealing $Li_7P_3S_{11}$ glass (denoted as Li7-glass) at 260 °C for different durations from 5 min to 24 h (denoted as Li7-5 min, Li7-1 h, and Li7-24 h respectively). As-prepared Li7-glass exhibits broad diffraction features without distinct Bragg peaks (Fig. 4a), consistent with an amorphous structure. Upon annealing, emergence of diffraction peaks is observed even after short annealing durations (5 min), indicating the onset of crystallization, and the peaks can be attributed to the metastable triclinic $Li_7P_3S_{11}$ phase (space group: $P\overline{1}$), in agreement with previous reports [44]. Apparent increase in the peak intensity can be observed after annealing for 1 h (Li-1 h), however, further annealing to 24 h led to the formation of $Li_4P_2S_6$ (Fig. 4a) [42,44]. The structural evolution can be observed from Raman spectra

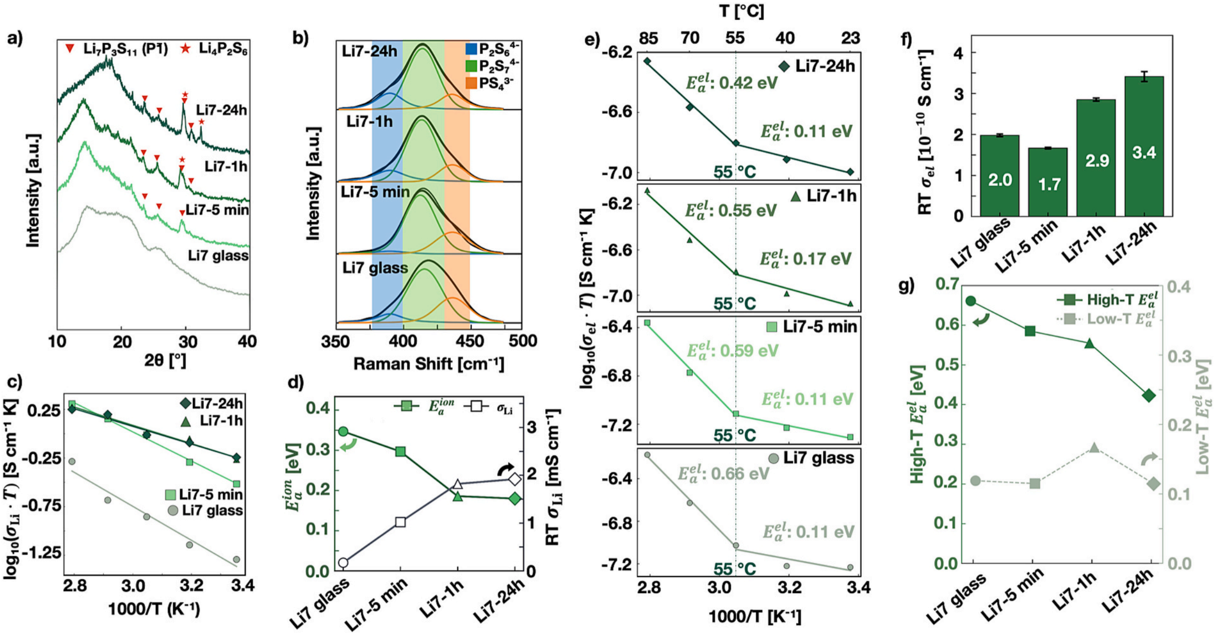

Fig. 4. Effect of annealing on the transport properties of $Li_7P_3S_{11}$ glass and glass-ceramics. X-ray diffraction (a), Raman spectra (b), Arrhenius plot of ionic conductivity (c), room temperature ionic conductivity and activation energy for ionic transport (d), Arrhenius plots of electronic conductivity (e), room temperature ionic conductivity (f), activation energy for electronic transport (f) of $Li_7P_3S_{11}$ glass and glass-ceramics with various crystallinity.

(Fig. 4b). The as-prepared Li7-glass displays peaks centered at approximately 425, 410, and 390 cm^{-1}, commonly assigned to PS_4^{3-}, $P_2S_7^{4-}$, and $P_2S_6^{4-}$ units, respectively, in agreement with previous reports [42,44]. Upon short-duration annealing (Li7-5 min), a reduction in the intensity of the $P_2S_6^{4-}$ peak is observed, accompanied by an increase in the $P_2S_7^{4-}$ unit. A slight increase in the peak intensity of $P_2S_6^{4-}$ can be observed for Li-24 h (Fig. 4b), consistent with the formation of $Li_4P_2S_6$ phase from the XRD results (Fig. 4a) after prolonged annealing. Fig. 4c and d show the effect of the annealing on the ionic transport property. A monotonic increase in the room temperature σ_{Li} from 1.02 to 1.92 mS cm^{-1} is observed with annealing duration, with a decrease in activation energy from 0.347 to 0.180 eV (Fig. 4d). The similar ionic transport property of Li7-24 h when comparing with Li7-1 h suggests that the enhancement of ionic transport by improving the crystallinity through extended annealing is compensated by the formation of a poorly conducting $Li_4P_2S_6$ phase.

The Arrhenius plots of σₑ for Li7-glass and its corresponding glass-ceramics are shown in Fig. 4e. For Li7 glass, the activation energy in the high-temperature regime is 0.66 eV and 0.11 eV in the low-temperature regime (Fig. 4e). The as-prepared Li7-glass exhibits an σ_{el} of approximately 2.0×10^{-10} S cm^{-1} (Fig. 4f). Upon short-duration annealing (Li7-5 min), a slight decrease in room-temperature σₑ is observed. Further annealing leads to a systematic increase in σ_{el}, reaching 2.9×10^{-10} S cm^{-1} for Li7-1 h and 3.4×10^{-10} S cm^{-1} for Li7-24 h (Fig. 4f). With increasing annealing duration, the high-temperature E_a^{el} decreases monotonically, from 0.59 eV (Li7-5 min) to 0.55 eV (Li7-1 h) and 0.42 eV (Li7-24 h) (Fig. 4g). In contrast, the low-temperature apparent activation energy remains relatively low across all annealed samples, clustering near 0.11–0.17 eV, with no clear monotonic trend. Different from the activation energy results for Li_3PS_4 (Fig. 3g), the high-temperature and low-temperature E_a^{el} for $Li_7P_3S_{11}$ do not exhibit the trend with the annealing durations (Fig. 4g). Overall, in spite of a slight decrease in σ_{el} for Li7-5 min, the annealing process, which is required to achieve high ionic conductivity of $Li_7P_3S_{11}$ glass-ceramics, may lead to enhancement of the electronic transport properties.

2.4. Effect of Cl$^-$ doping on electronic transport in Li_3PS_4 glasses

To gain further insight into the electronic transport mechanisms, we investigated the effect of doping on the electronic transport properties of Li_3PS_4 glasses. Cl$^-$ and N^{3-} were selected as the dopants to create Li-poor and Li-rich thiophosphate glasses, respectively. Li_3PS_4 glasses with various Cl$^-$ doping contents were synthesized by the high-energy ball milling of Li_2S, P_2S_5 and LiCl based on the composition, $Li_{3\text{-}4x}PS_{4\text{-}4x}Cl_{4x}$, where x = 0, 1, 3 or 5% (denoted as Li3-glass, LiCl-1%, LiCl-3%, and LiCl-5%). No discernible Bragg peaks can be observed from the XRD of all SEs (Fig. 5a), consistent with retention of an amorphous structure. No peaks associated with LiCl were observed either, suggesting complete dissolution and incorporation in the glass network. In the case of Raman spectra (Fig. 5b), at higher dopant concentrations, an additional peak near 410 cm^{-1}, commonly assigned to $P_2S_7^{4-}$ units, emerges in LiCl-3% and increases in intensity in LiCl-5%. These changes are correlated with an apparent, marginal decrease in the PS_4^{3-} peak, possibly related to the decrease of Li content in the glasses. For Cl-doped samples, the room-temperature ionic conductivity increases sharply to 0.43 mS cm^{-1} for LiCl-1%, followed by a decrease to 0.18 and 0.17 mS cm^{-1} for LiCl-3% and LiCl-5%, respectively (Fig. 5c and d). The corresponding activation energies for ionic conductivity also display a non-monotonic dependence, decreasing to 0.27 eV for LiCl-1%, increasing to 0.36 eV for LiCl-3%, and decreasing again to 0.32 eV for LiCl-5% (Fig. 5d).

The Arrhenius plots of electronic conductivity Cl-doped Li_3PS_4 can also be separated into two regimes (Fig. 5e). Nevertheless, an apparent increase in the transition temperature that separates these two regimes can be observed for LiCl-3% and LiCl-5%. The localized state that dominates the hopping mechanism in the low-temperature regime can be equilibrated at a slightly higher temperature. The high-temperature activation energy ranges from 0.52 to 0.56 eV, while the low-temperature activation energy varies from 0.16 to 0.31 eV. The room-temperature σ_{el} increases monotonically with increasing Cl content, rising from 0.9×10^{-10} S cm^{-1} for undoped Li3 glass to 2.4×10^{-10}, 2.8×10^{-10}, and 3.5×10^{-10} S cm^{-1} for LiCl-1%, LiCl-3%, and LiCl-5%, respectively (Fig. 5f). The high-temperature activation energy exhibits a minor, but monotonically increasing trend with LiCl content, increasing from 0.52 eV for Li_3PS_4 glass to 0.53 eV, 0.54 eV and 0.56 eV for LiCl-

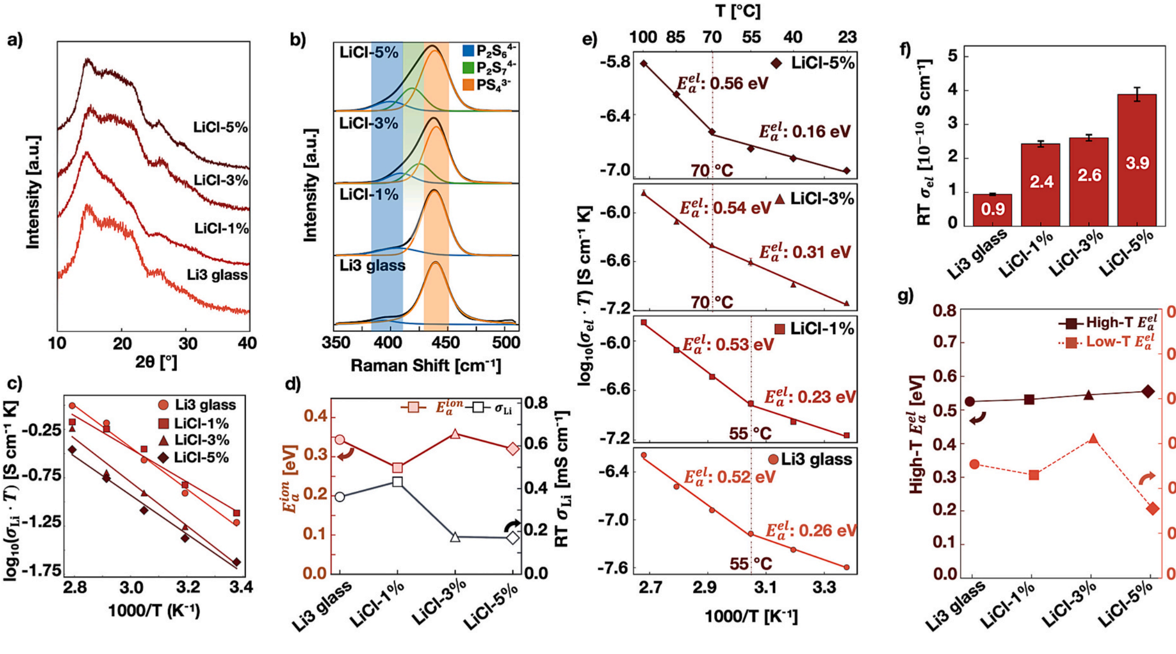

Fig. 5. Effect of Cl$^-$ doping on the transport properties of Li_3PS_4 glasses. X-ray diffraction (a), Raman spectra (b), Arrhenius plot of ionic conductivity (c), room temperature ionic conductivity and activation energy for ionic transport (d), Arrhenius plots of electronic conductivity (e), room temperature electronic conductivity (f), and activation energy for electronic transport (f) of Li_3PS_4 glasses with various Cl$^-$ doping contents.

1%, LiCl-3% and LiCl-5%, respectively (Fig. 5g). In contrast, no apparent trend can be observed for the low-temperature activation energies, varying from 0.23 to 0.31 eV (for Li3-glass, LiCl-1% and LiCl-3%) to 0.16 eV for LiCl-5% (Fig. 5g). Therefore, Cl-doping is associated with a systematic increase in room-temperature σ_e and a progressive increase in high-temperature E_a^{el} at higher dopant concentrations. The electronic conductivity and activation energy do not follow a typical inverse relationship that describes charge transport in solids, i.e., an increase in conductivity with a decrease in activation energy, suggesting the pre-exponential factor also plays an important role in governing electronic transport in these glasses [51,52].

2.5. *Effect of N^{3-} doping on electronic transport of Li_3PS_4 glasses*

Li_3PS_4 glasses with various N^{3-} doping contents were synthesized by high-energy ball milling of Li_2S, P_2S_5 and LiCl based on the composition, $Li_{3+4y}PS_{4-4y}N_{4y}$, where y = 0, 1, 3 or 5%. The XRD results in Fig. 6a suggest all samples retain an amorphous structure across all dopant concentrations. No peaks associated with Li_3N were observed either, suggesting complete dissolution and incorporation in the glass network. Raman spectra (Fig. 6b) show increases in the $P_2S_6^{4-}$ peak intensity with increasing N content, without discernible $P_2S_7^{4-}$ formation. N-doped glass samples show an opposite trend in room-temperature ionic conductivity compared to LiCl doping (Fig. 6c). The conductivity initially decreases to 0.23 mS cm^{-1} for Li3N-1%, followed by an increase to 0.25 and 0.40 mS cm^{-1} for Li3N-3% and Li3N-5%, respectively. The associated activation energies increase initially to 0.41 eV at a low Li_3N content and subsequently decrease to 0.35 and 0.27 eV for Li3N-3% and Li3N-5%, respectively (Fig. 6d).

Fig. 6e shows the Arrhenius plot of electronic conductivity in N-doped Li_3PS_4 glasses. The room-temperature σ_{el} compiled in Fig. 6f, increases strongly with increasing Li_3N content, rising from 0.9×10^{-10} S cm^{-1} for undoped Li3 glass to 2.5×10^{-10}, 3.8×10^{-10}, and 8.6×10^{-10} S cm^{-1} for Li3N-1%, Li3N-3%, and Li3N-5%, respectively. The increase of σ_{el} is also accompanied by an overall decrease in both high-temperature activation energy from 0.52 to 0.33 eV and low-temperature activation energy from 0.26 to 0.18 eV with the increase of dopant concentration (Fig. 6g).

2.6. *Comparison of electronic transport properties across processing conditions and compositions*

The results we collected also allow us to compare the electronic transport properties, including σ_{el} at RT and 85 °C, as well as E_a^{el} in the high-temperature and low-temperature regimes across the annealing and doping conditions (Fig. 7). Firstly, it is unfortunate to note that almost all processing and doping conditions may lead to increase in the room temperature σ_{el} when compared to baseline Li_3PS_4 glass (Fig. 7a). N-doping leads to the largest enhancement in the room temperature σ_{el}, followed by Cl-doping and annealing (Fig. 7a). The σ_{el} at 85 °C (Fig. 7b) generally follow the same trend with few deviations (Li3-24 h, LiCl-5%, and Li3N-3%). Secondly, while annealing Li_3PS_4 glasses for 5 min increases the σ_{el} at RT, no apparent variations can be observed for extending annealing to 1 and 24 h. While increasing the annealing durations of $Li_7P_3S_{11}$ glasses leads to slight increase in the σ_{el} at RT, no apparent trend can be observed for σ_{el} at 85 °C. The results suggest that the well-documented trend for ionic conductivity evolution during annealing is not applicable to electronic transport properties. No apparent correlation between the evolution of electronic and ionic conductivities can be observed as well (Fig. S12), indicative of different mechanisms of ionic and electronic transport in these SEs. No apparent temperature dependence of the activation energy for ionic transport can be observed for all SEs within the investigated temperature range. While it is not expected that ionic transport and electronic transport in Li solid electrolytes are governed by the same point defects, the results highlight the challenges of understanding electronic transport and conduction mechanisms based on conventional wisdom learned from ionic transport. Common design approaches to improve the ionic conductivity may not work for reducing the electronic conductivity.

All the SEs exhibited a lower E_a^{el} in the low-temperature regime than in the high-temperature regime (Fig. 7c and d), indicative of a generally weaker hopping process at lower temperatures as a generalized phenomenon for lithium thiophosphate glasses and glass-ceramics. Different from ionic transport properties (Fig. S12), no inverse correlation between the activation energies and electronic conductivity can be observed, except for N-doped Li_3PS_4 glasses, indicative of a strong contribution from the pre-exponent in governing values [52]. The

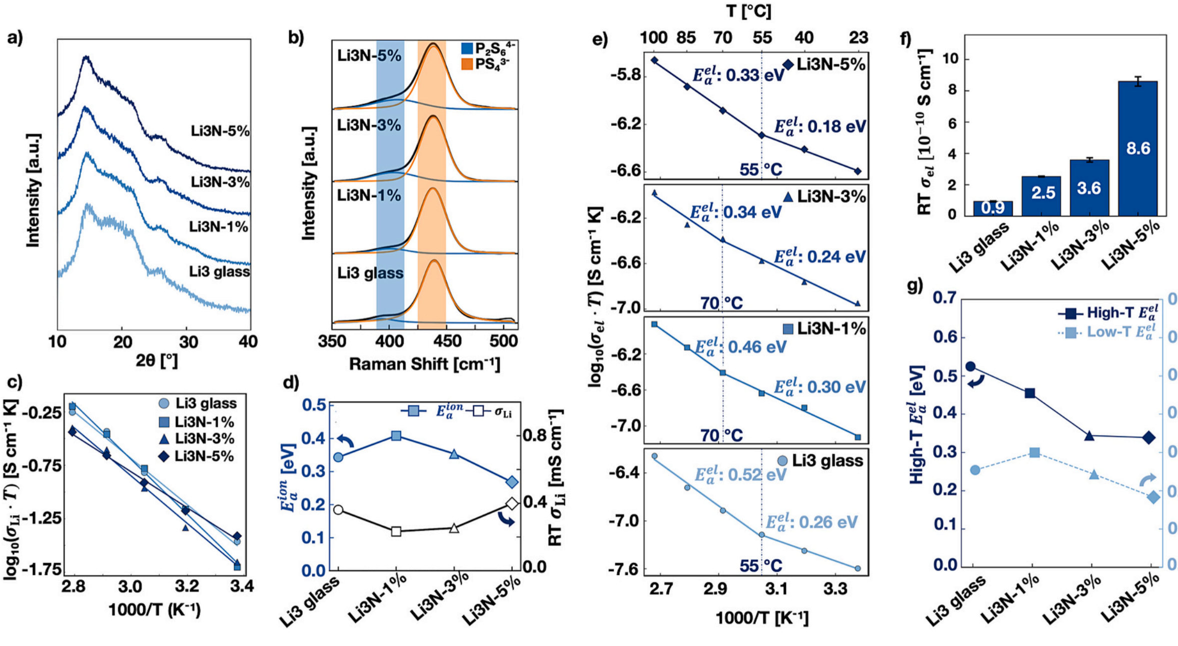

Fig. 6. Effect of N^{3-} doping on the transport properties of Li_3PS_4 glasses. X-ray diffraction (a), Raman spectra (b), Arrhenius plot of ionic conductivity (c), room temperature ionic conductivity and activation energy for ionic transport (d), Arrhenius plots of electronic conductivity (e), room temperature electronic conductivity (f), and activation energy for electronic transport (g) of Li_3PS_4 glasses with various N^{3-} doping contents.

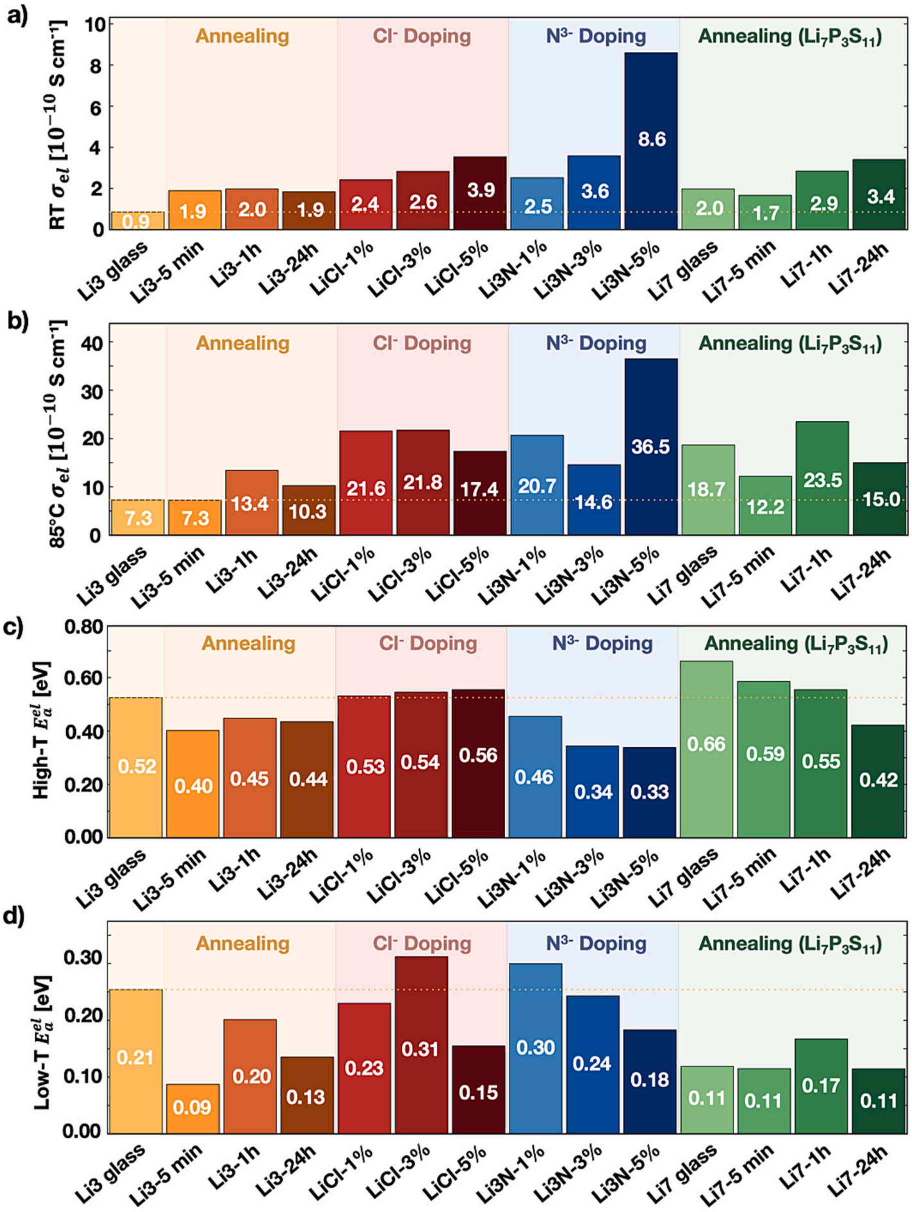

Fig. 7. Comparison of electronic transport properties across processing conditions and compositions. Electronic conductivity at room temperature (a) and 85 °C (b) and activation energy of electronic conductivity for the high-temperature regime (c) and the low-temperature regime (d).

average of the high-temperature E_a^{el} for SEs at the same condition decreases from Cl-doping (0.54 eV), $Li_7P_3S_{11}$ annealing (0.52 eV), Li_3PS_4 annealing (0.43 eV) to N-doping (0.38 eV), while the average of the low-temperature E_a^{el} ranks N-doping (0.24 eV)= Cl-doping (0.24 eV) > Li_3PS_4 annealing (0.14 eV) > $Li_7P_3S_{11}$ annealing (0.13 eV). The inconsistent order for the two E_a^{el} may also imply two independent hopping mechanisms in the high-temperature and low-temperature regimes.

Overall, N^{3-} doping is found to have the largest effect in enhancing electronic transport properties. Compared with the baseline Li_3PS_4 glass, σ_{el} increases by a factor of 9.6 at RT and by a factor of 5.0 at 85 °C, accompanied by a decrease in E_a^{el} from 0.52 to 0.33 eV in the high-temperature regime and from 0.21 to 0.18 eV in the low-temperature regime. Based on a previous study on the defect chemistry and transport mechanism of Li_2S, the introduction of negative dopants such as Li_3N in Li_2S, will lead to the formation of holes [53]. The clear trend of electronic transport properties in N-doped lithium thiophosphate SEs also implies holes, instead of electrons, as the possible dominant charge carrier for electronic transport in Li_3PS_4. It is hypothesized that the introduced N^{3-} can attract holes, forming localized states within the bandgap for the hopping process [50].

The results also highlight the knowledge gap in understanding the electronic transport mechanisms in lithium thiophosphate glass and glass-ceramic solid electrolytes. Many questions remain to be answered. The origin of the temperature-dependent activation energy is not clear. Nevertheless, the decrease in activation energy for electronic transport at lower temperatures has been widely reported for semiconductor glasses, where several weak hopping processes (e.g., small polaron hopping, variable range polaron hopping) at lower temperatures have been proposed [54–61]. More careful study of the relationship between the electronic conductivity and temperature over a wider temperature range may be helpful to understand the similarities and differences of the hopping mechanism between semiconductor glasses and ionic glasses. A recent computational study from Demir et al [62] suggested small polaron hopping as the electron transport mechanism in single-crystal $Li_7P_3S_{11}$. The authors further proposed that the "small electron polaron" is localized on a PS_4^{3-} structural unit while the "small hole polaron" is located on $P_2S_7^{4-}$ polyhedra [62]. The existence of small polarons also lowers the barrier to delocalize the charge between two sites to 0.4 eV [62], which is similar to what we observe in the high-temperature regime. However, the trend between the electronic conductivity and the contents of PS_4^{3-}, $P_2S_6^{4-}$ or $P_2S_7^{4-}$ structural units in the glass and glass-ceramics studied in this work appear to be convoluted (Fig. S13).

It has also been reported, through first-principles defect calculation, that the formation of native point defects can play an important role in providing electronic carriers and lowering the energy barrier for electronic transport [49,63,64]. Given the large effect of N-doping on the electronic transport properties, we would also like to highlight the critical role of extrinsic defects, for example from impurities, surfaces, or grain boundaries [65]. As the defect chemistry is very sensitive to impurity, even a slight amount of impurity, from the reactants or processing, may lead to significant enhancements in electronic transport properties [53]. Alt et al. proposed the effect of Li_2O impurity on the electronic transport property of lithium halides [17]. Inspired by a computational study from Tian et al [66] that highlighted the important role of surfaces in promoting electronic transport in β-Li_3PS_4, we also tried to measure the electronic conductivity of Li_3PS_4 glasses fabricated by cold-pressing SE powders at various pressures to see if there is any correlation between the measured electronic conductivity and porosity. However, no repeatable results were obtained, probably due to the large uncertainty in controlling the contact between the SS electrode and the porous SE. The results are therefore not included here. It should also be noted that uncertainty remains for DC polarization of double-blocking-electrode cells with controlled voltage and durations, such as the contact overpotential between the electrode and SE. A four-probe setup with four blocking electrodes may be helpful to mitigate the effects of the contact overpotential [67]. More careful characterizations of the localized defect states, for example by diffuse reflectance UV–vis spectroscopy [49] or photoluminescence spectroscopy [17] may also provide critical insights into identifying possible defects that governs electronic transport in the SEs.

We would also like to note that while double-blocking-electrode cells were proposed as a more reasonable approach over Hebb-Wagner cells to determine the intrinsic electronic transport in lithium thiophosphate solid electrolytes, it does not mean this applies to other types of SEs. For more electrochemically stable SEs such as oxides or halides, Hebb-Wagner method is still the most powerful technique to determine the electronic transport properties, including both electron transport and hole transport over a wide range of Li activities. Therefore, a more cogent explanation is that the method to be used to determine the intrinsic electronic conductivity in the SEs depends on the electrochemical stability of the SEs. Since double-blocking cells can also be used to probe the electronic conductivity at a certain Li activity, it would be intriguing to compare it to the value measured by Hebb-Wagner method at the same Li activity.

3. Conclusions

Due to unavoidable anodic decomposition during Hebb-Wagner polarization measurements, we propose double-blocking-electrode polarization as a more appropriate method to determine the intrinsic electronic transport properties of lithium thiophosphate-based SEs. Deriving from a diffusion-driven electronic transport mechanism, the average σ_{el} measured from the double-blocking-electrode polarization is equivalent to the σ_{el} at a certain Li activity related to the initial Li activity of unpolarized SEs. Using this method, we benchmark the electronic transport properties of common Li thiophosphate glass and glass-ceramic SEs, including Li_3PS_4 and $Li_7P_3S_{11}$ glasses, Li_3PS_4 and $Li_7P_3S_{11}$ glass-ceramics with varying crystallinity, as well as Cl-doped and N-doped Li_3PS_4 glasses with varying dopant concentrations at different temperatures from 23 to 85 °C (or 100 °C). The results allow us to investigate the effect of annealing and doping on the electronic transport properties of lithium thiophosphate SEs. It was found that all annealing and doping conditions will lead to enhancements in σ_{el} when compared with the baseline Li_3PS_4 and $Li_7P_3S_{11}$ glass SEs, with N-doping exhibiting the largest enhancement in room temperature σ_{el} from 0.9×10^{-10} to 8.6×10^{-10} S cm^{-1} (after introducing 5% Li_3N in Li_3PS_4). As the introduction of N^{3-} will likely generate point defects with positive charge, holes instead of electrons are suggested as the dominant electronic carriers under the measured conditions. There is a correlation between the various structural units and the electronic conductivity. However, it appears to be convoluted, and we are cautious to draw any definitive conclusions. All SEs studied in this work exhibit two distinct linear regimes in the Arrhenius plots of σ_{el}; a high-temperature regime with an activation energy ranging from 0.33 to 0.66 eV and a low-temperature regime with activity energy ranging from 0.09 to 0.31 eV, suggesting temperature dependence of the hopping mechanism for electronic transport. No apparent correlation between electronic and ionic transport can be observed by changing the processing and doping conditions. Our findings highlight the challenges in understanding and suppressing partial electronic transport in lithium thiophosphate SEs. We hope that our experimental data on the electronic transport properties of a wide range of lithium thiophosphate SEs will establish crucial benchmark parameters for upcoming experimental and computational studies on this largely ignored topic.

4. Experimental

4.1. Materials synthesis

Lithium thiophosphate SEs were prepared by high-energy planetary ball milling (Retsch PM100/PM200) of a 3.6 g mixture of Li_2S (99.98% trace metals basis; Sigma-Aldrich) and P_2S_5 (99%; Sigma-Aldrich) in appropriate stoichiometric ratios (3:1 for Li_3PS_4 glass and 7:3 for $Li_7P_3S_{11}$ glass). Milling was carried out for 100 h in zirconia jars at 510 rpm using 10 zirconia balls for Li_3PS_4 and 15 zirconia balls for $Li_7P_3S_{11}$. To obtain the corresponding glass-ceramics, approximately 1 g of the as-prepared glass was sealed in quartz tubes and annealed in a box furnace (Lindberg Blue M). Li_3PS_4 glass samples were annealed at 200 °C for 5 min, 1 h, or 24 h, while $Li_7P_3S_{11}$ glass samples were annealed at 260 °C for the same durations. Cl-doped Li_3PS_4 glass samples were prepared by ball milling a ~ 3.6 g mixture of Li_2S, P_2S_5, and LiCl (99.9%; Thermo Scientific) such that the final stoichiometry was $Li_{3\text{-}4x}PS_{4\text{-}4x}Cl_{4x}$, where x = 1, 3 or 5 mol% (LiCl). Similarly, Li_3PS_4 glass samples doped with Li_3N (99.4%; Thermo Scientific) were prepared using mixtures of Li_2S, P_2S_5, and Li_3N to obtain a final stoichiometry of $Li_{3+4y}PS_{4\text{-}4y}N_{4y}$, where y = 1, 3 or 5 mol% (Li_3N). All doped compositions were milled for 100 h in zirconia jars at 510 rpm using 10 zirconia balls. All sample handling was performed either under vacuum or in an argon-filled inert atmosphere.

4.2. Materials characterization

Powder X-ray diffraction (XRD) measurements were performed using a diffractometer equipped with a Cu Kα radiation source (Malvern PANalytical X'Pert). Samples were loaded onto fiberglass sample holders and sealed with kapton tape to prevent air exposure during measurement. Raman spectroscopy was conducted using a confocal Raman microscope with a 532 nm laser source (Renishaw). Samples were mounted on glass slides, covered with a glass coverslip, and sealed with transparent tape prior to measurement.

4.3. Cell fabrication

Double-blocking-electrode cells were fabricated by cold-pressing 150 mg of SE powder at 400 MPa for 3 min between two stainless steel ion-blocking electrodes, which also served as current collectors.

The assembled cell was subsequently clamped tightly to maintain mechanical contact during measurements. The assembly was placed and sealed in a glass jar with external current leads to prevent exposure to air and moisture.

4.4. *Electronic conductivity measurements*

DC polarization measurements were performed using an electrochemical workstation (BioLogic VSP-3 potentiostat) equipped with an ultra-low-current module (BioLogic ULC300; base current ~1 pA) to enable reliable detection of small electronic currents. The measurement electronics was placed inside a Faraday cage to minimize electromagnetic interference. The assembled double-blocking-electrode cells were placed inside an oven (VWR Forced Air) that also served as a Faraday cage. DC polarization was conducted at an applied potential of 0.3 V for 12 h at each measurement temperature (23, 40, 55, 70, and 85 °C; 100 °C where applicable). Steady-state currents were extracted by averaging the final ten data points of each current-time curve, corresponding to the last 5 min of each measurement.

4.5. *Ionic conductivity measurements*

AC impedance spectroscopy measurements were performed using an electrochemical workstation (BioLogic VSP-3 potentiostat). The measurement electronics was placed inside a Faraday cage to minimize electromagnetic interference. The assembled double-blocking-electrode cells were placed inside an oven (VWR Forced Air) that also served as a Faraday cage. Impedance spectra were collected using a small-signal AC perturbation of 10 mV over a frequency range from 1 mHz to 7 MHz at each measurement temperature (23, 40, 55, 70, and 85 °C).

CRediT authorship contribution statement

Ratnottam Das: Writing – review & editing, Writing – original draft, Validation, Methodology, Investigation, Formal analysis, Data curation, Conceptualization. **Ruihao Deng:** Methodology, Investigation, Data curation. **Sara Seelman:** Investigation, Data curation. **Keng Xu:** Methodology, Investigation, Data curation. **Alisha Toporski:** Investigation, Data curation. **Ru Xiao:** Investigation, Data curation. **Ruixin Wu:** Investigation, Data curation. **Fudong Han:** Writing – review & editing, Writing – original draft, Supervision, Resources, Project administration, Methodology, Funding acquisition, Formal analysis, Conceptualization.

Declaration of generative AI and AI-assisted technologies in the writing process

Not applicable.

Declaration of competing interest

The authors declare that they have no known competing financial interests or personal relationships that could have appeared to influence the work reported in this paper.

Acknowledgements

The authors acknowledge the support from the US National Science Foundation (Award No. 2238672). F.H. also acknowledges the support from the Priti and Mukesh Chatter Career Development Chair Professorship at the Rensselaer Polytechnic Institute (RPI). We would like to thank the characterization facilities in the RPI Nanoscale Characterization Core, operated by the Center for Materials, devices and Integrated Systems at RPI.

Appendix A. Supplementary data

Supplementary data to this article can be found online at https://doi.org/10.1016/j.ssi.2026.117265.

Data availability

Data will be made available on request.

References

[1] J. Maier, Physical Chemistry of Ionic Materials: Ions and Electrons in Solids, Wiley, Hoboken, 2004.

[2] W. Weppner, R.A. Huggins, Electrochemical methods for determining kinetic properties of solids, Annu. Rev. Mater. Sci. 8 (1978) 269–311, https://doi.org/10.1146/annurev.ms.08.080178.001413.

[3] S. Bredikhin, Electronic conductivity and current instability in superionic crystals, Solid State Ion. 81 (1995) 19–28, https://doi.org/10.1016/0167-2738(95)00153-w.

[4] K. Minami, F. Mizuno, A. Hayashi, M. Tatsumisago, Lithium ion conductivity of the $Li_2S–P_2S_5$ glass-based electrolytes prepared by the melt quenching method, Solid State Ion. 178 (2007) 837–841, https://doi.org/10.1016/j.ssi.2007.03.001.

[5] S. Ujiie, T. Inagaki, A. Hayashi, M. Tatsumisago, Conductivity of 70 Li_2S ·30 P_2S_5 glasses and glass–ceramics added with lithium halides, Solid State Ion. 263 (2014) 57–61, https://doi.org/10.1016/j.ssi.2014.05.002.

[6] H. Tsukasaki, S. Mori, S. Shiotani, H. Yamamura, Ionic conductivity and crystallization process in the $Li_2S–P_2S_5$ glass electrolyte, Solid State Ion. 317 (2018) 122–126, https://doi.org/10.1016/j.ssi.2018.01.010.

[7] H.J. Deiseroth, S. Kong, H. Eckert, J. Vannahme, C. Reiner, T. Zaiß, M. Schlösser, Li_6PS_5X: a class of crystalline Li-rich solids with an unusually high Li^+ mobility, Angew. Chem. 47 (2008) 755–758, https://doi.org/10.1002/anie.200703900.

[8] N. Kamaya, K. Homma, Y. Yamakawa, M. Hirayama, R. Kanno, M. Yonemura, T. Kamiyama, Y. Kato, S. Hama, K. Kawamoto, A. Mitsui, A lithium superionic conductor, Nat. Mater. 10 (2011) 682–686, https://doi.org/10.1038/nmat3066.

[9] B. Shao, Y. Huang, F. Han, Electronic conductivity of lithium solid electrolytes, Adv. Energy Mater. 13 (2023) 2204098, https://doi.org/10.1002/aenm.202204098.

[10] R. Deng, R. Das, R. Wu, K. Xu, B. Shao, F. Han, Understanding calendar aging of thiophosphate-based solid-state batteries, J. Electrochem. Soc. 172 (2025) 100519, https://doi.org/10.699149/1945-7111/ae0f59.

[11] I. Kochetkov, T.-T. Zuo, R. Ruess, B. Singh, L. Zhou, K. Kaup, J. Janek, L. Nazar, Different interfacial reactivity of lithium metal chloride electrolytes with high voltage cathodes determines solid-state battery performance, Energ. Environ. Sci. 15 (2022) 3933–3944, https://doi.org/10.1039/d2ee00803c.

[12] C.D. Alt, Nadia U.C.B. Müller, L.M. Riegger, Burak Aktekin, P. Minnmann, K. Peppler, J. Janek, Quantifying multiphase SEI growth in sulfide solid electrolytes, Joule 8 (2024) 2755–2776, https://doi.org/10.1016/j.joule.2024.07.006.

[13] S. Wenzel, D.A. Weber, T. Leichtweiss, M.R. Busche, J. Sann, J. Janek, Interphase formation and degradation of charge transfer kinetics between a lithium metal anode and highly crystalline $Li_7P_3S_{11}$ solid electrolyte, Solid State Ion. 286 (2016) 24–33, https://doi.org/10.1016/j.ssi.2015.11.034.

[14] F. Han, A.S. Westover, J. Yue, X. Fan, F. Wang, M. Chi, D.N. Leonard, N.J. Dudney, H. Wang, C. Wang, High electronic conductivity as the origin of lithium dendrite formation within solid electrolytes, Nat. Energy 4 (2019) 187–196, https://doi.org/10.1038/s41560-018-0312-z.

[15] T. Krauskopf, F.H. Richter, W.G. Zeier, J. Janek, Physicochemical concepts of the lithium metal anode in solid-state batteries, Chem. Rev. 120 (2020) 7745–7794, https://doi.org/10.1021/acs.chemrev.0c00431.

[16] L.C. De Jonghe, Transport number gradients and solid electrolyte degradation, J. Electrochem. Soc. 129 (1982) 752–755, https://doi.org/10.1149/1.2123965.

[17] C.D. Alt, J. Kessler-Kühn, J.K. Eckhardt, M. Stein, S. Chatterjee, M.T. Elm, J. Janek, The partial electronic conductivity of lithium halides and their role in SEI formation in solid-state batteries – Hebb-Wagner-type measurements, Solid State Ion. 429 (2025) 116991, https://doi.org/10.1016/j.ssi.2025.116991.

[18] C.D. Alt, J. Janek, Quantifying the self-discharge rate of solid-state batteries, Nat. Energy (2026) 1–6, https://doi.org/10.1038/s41560-026-02038-1.

[19] C. Wagner, Galvanic cells with solid electrolytes involving ionic and electronic conduction, in: Proceedings of International Committee of Electrochemical Thermodynamics and Kinetics (CITCE), 7th Meeting, Butterworth Scientific Publisher, London, 1957, pp. 361–377.

[20] M.H. Hebb, Electrical conductivity of silver sulfide, J. Chem. Phys. 20 (1952) 185–190, https://doi.org/10.1063/1.1700165.

[21] C. Wagner, Galvanische zellen mit festen elektrolyten mit gemischter stromleitung, Z. Elektrochem. Ber. Bunsenges. Phys. Chem. 60 (1956) 4–7, https://doi.org/10.1002/bbpc.19560600104.

[22] J.B. Wagner, C. Wagner, Electrical conductivity measurements on cuprous halides, J. Chem. Phys. 26 (1957) 1597–1601, https://doi.org/10.1063/1.1743590.

[23] J. Maier, G. Schwitzgebel, Electrochemical polarization of orthorhombic PbO, Mater. Res. Bull. 18 (1983) 601–608, https://doi.org/10.1016/0025-5408(83)90218-0.

[24] J. Maier, Conductivity in an activity gradient, J. Phys. Chem. Solid 46 (1985) 197–200, https://doi.org/10.1016/0022-3697(85)90034-4.

[25] W. Weppner, J. Liu, Polarization studies of the electronic minority charge carriers in Ag^{+} $-\beta''$-alumina, Zeitschrift Für Naturforschung A. 46 (1991) 409–415, https://doi.org/10.1515/zna-1991-0506.

[26] F. Han, Y. Zhu, X. He, Y. Mo, C. Wang, Electrochemical stability of $Li_{10}GeP_2S_{12}$ and $Li_7La_3Zr_2O_{12}$ solid electrolytes, Adv. Energy Mater. 6 (2016) 1501590, https://doi.org/10.1002/aenm.201501590.

[27] F. Han, T. Gao, Y. Zhu, K.J. Gaskell, C. Wang, A battery made from a single material, Adv. Mater. 27 (2015) 3473–3483, https://doi.org/10.1002/adma.201500180.

[28] W.D. Richards, L.J. Miara, Y. Wang, J.C. Kim, G. Ceder, Interface stability in solid-state batteries, Chem. Mater. 28 (2015) 266–273, https://doi.org/10.1021/acs.chemmater.5b04082.

[29] Y.-Z. Zhu, X. He, Y. Mo, Origin of outstanding stability in the lithium solid electrolyte materials: insights from thermodynamic analyses based on first-principles calculations, ACS Appl. Mater. Interfaces 7 (2015) 23685–23693, https://doi.org/10.1021/acsami.5b07517.

[30] I. Riess, R. Safadi, Failure of Hebb-Wagner polarization measurements due to decomposition of the sample, Solid State Ion. 59 (1993) 99–108, https://doi.org/10.1016/0167-2738(93)90235-u.

[31] I. Riess, Review of the limitation of the Hebb-Wagner polarization method for measuring partial conductivities in mixed ionic electronic conductors, Solid State Ion. 91 (1996) 221–232, https://doi.org/10.1016/s0167-2738(96)83022-0.

[32] I. Riess, R. Safadi, H.L. Tuller, Problems with Hebb-Wagner polarization measurements due to overpotentials and decomposition of the sample, Solid State Ion. 72 (1994) 3–6, https://doi.org/10.1016/0167-2738(94)90116-3.

[33] B.J. Neudecker, W. Weppner, Li_9SiAlO_8: a lithium ion electrolyte for voltages above 5.4 V, J. Electrochem. Soc. 143 (1996) 2198–2203, https://doi.org/10.1149/1.1836980.

[34] G. Liu, W. Weng, Z. Zhang, L. Wu, J. Yang, X. Yao, Densified Li_6PS_5Cl nanorods with high ionic conductivity and improved critical current density for all-solid-state lithium batteries, Nano Lett. 20 (2020) 6660–6665, https://doi.org/10.1021/acs.nanolett.0c02489.

[35] T. Ohtomo, F. Mizuno, A. Hayashi, K. Tadanaga, M. Tatsumisago, Electrical and electrochemical properties of Li_2S–P_2S_5–P_2O_5 glass–ceramic electrolytes, J. Power Sources 146 (2005) 715–718, https://doi.org/10.1016/j.jpowsour.2005.03.063.

[36] L. Zhou, K.-H. Park, X. Sun, F. Lalère, T. Adermann, P. Hartmann, L.F. Nazar, Solvent-engineered design of argyrodite Li_6PS_5X ($X = Cl, Br, I$) solid electrolytes with high ionic conductivity, ACS Energy Lett. 4 (2018) 265–270, https://doi.org/10.1021/acsenergylett.8b01997.

[37] G. Liu, J. Shi, M. Zhu, W. Weng, L. Shen, J. Yang, X. Yao, Ultra-thin free-standing sulfide solid electrolyte film for cell-level high energy density all-solid-state lithium batteries, Energy Storage Mater. 38 (2021) 249–254, https://doi.org/10.1016/j.ensm.2021.03.017.

[38] C. Dietrich, D. Weber, S.J. Sedlmaier, S. Indris, S.P. Culver, D. Walter, J. Janek, W. G. Zeier, Lithium ion conductivity in Li_2S–P_2S_5 glasses – building units and local structure evolution during the crystallization of superionic conductors Li_3PS_4, $Li_7P_3S_{11}$ and $Li_4P_2S_7$, J. Mater. Chem. A 5 (2017) 18111–18119, https://doi.org/10.1039/c7ta06067j.

[39] H. Stöffler, T. Zinkevich, M. Yavuz, A.-L. Hansen, M. Knapp, J. Bednarčík, S. Randau, F.H. Richter, J. Janek, H. Ehrenberg, S. Indris, Amorphous versus crystalline Li_3PS_4: local structural changes during synthesis and Li ion mobility, J. Phys. Chem. C 123 (2019) 10280–10290, https://doi.org/10.1021/acs.jpcc.9b01425.

[40] F. Marchini, B. Porcheron, G. Rousse, L. Albero Blanquer, L. Droguet, D. Foix, T. Koç, M. Deschamps, J.M. Tarascon, The hidden side of nanoporous β-Li_3PS_4 solid electrolyte, Adv. Energy Mater. 11 (2021) 2101111, https://doi.org/10.1002/aenm.202101111.

[41] M. Takahashi, S. Yang, K. Yamamoto, K. Ohara, N.H.H. Phuc, T. Watanabe, T. Uchiyama, A. Sakuda, A. Hayashi, M. Tatsumisago, H. Muto, A. Matsuda, Y. Uchimoto, Improvement of lithium ionic conductivity of Li_3PS_4 through suppression of crystallization using low-boiling-point solvent in liquid-phase synthesis, Solid State Ion. 361 (2021) 115568, https://doi.org/10.1016/j.ssi.2021.115568.

[42] Y. Seino, M. Nakagawa, M. Senga, H. Higuchi, K. Takada, T. Sasaki, Analysis of the structure and degree of crystallisation of $70Li_2S$–$30P_2S_5$ glass ceramic, J. Mater. Chem. A 3 (2015) 2756–2761, https://doi.org/10.1039/c4ta04332d.

[43] K. Minami, A. Hayashi, M. Tatsumisago, Crystallization process for superionic $Li_7P_3S_{11}$ glass-ceramic electrolytes, J. Am. Ceram. Soc. 94 (2011) 1779–1783, https://doi.org/10.1111/j.1551-2916.2010.04335.x.

[44] M.R. Busche, D. Weber, Y. Schneider, C. Dietrich, S. Wenzel, T. Leichtweiß, D. Schröder, W. Zhang, H. Weigand, D. Walter, S.J. Sedlmaier, D. Houtarde, L. F. Nazar, J. Janek, *In situ* monitoring of fast Li-ion conductor $Li_7P_3S_{11}$ crystallization inside a hot-press setup, Chem. Mater. 28 (2016) 6152–6165, https://doi.org/10.1021/acs.chemmater.6b02163.

[45] A. Fukushima, A. Hayashi, H. Yamamura, M. Tatsumisago, Mechanochemical synthesis of high lithium ion conducting solid electrolytes in a Li_2S-P_2S_5-Li_3N system, Solid State Ion. 304 (2017) 85–89, https://doi.org/10.1016/j.ssi.2017.03.010.

[46] H. Näfe, M. Fritz, W.J. Lorenz, On the defect electron conduction parameter of Na-beta-alumina, Solid State Ion. 74 (1994) 275–278, https://doi.org/10.1016/0167-2738(94)90221-6.

[47] H. Näfe, Electronic conductivity of a solid oxide electrolyte in the low temperature range, Solid State Ion. 59 (1993) 5–15, https://doi.org/10.1016/0167-2738(93)90226-s.

[48] Y. Yang, Q. Wu, Y. Cui, Y. Chen, S. Shi, R.-Z. Wang, H. Yan, Elastic properties, defect thermodynamics, electrochemical window, phase stability, and Li^{+} mobility of Li_3PS_4: insights from first-principles calculations, ACS Appl. Mater. Interfaces 8 (2016) 25229–25242, https://doi.org/10.1021/acsami.6b06754.

[49] P. Gorai, T. Famprikis, B. Singh, V. Stevanović, P. Canepa, Devil is in the defects: electronic conductivity in solid electrolytes, Chem. Mater. 33 (2021) 7484–7498, https://doi.org/10.1021/acs.chemmater.1c02345.

[50] F.A. Kröger, H. Vink, Relations between the concentrations of imperfections in crystalline solids, Solid State Phys. 3 (1956) 307–435, https://doi.org/10.1016/s0081-1947(08)60135-6.

[51] R.B. Nuernberg, Numerical comparison of usual Arrhenius-type equations for modeling ionic transport in solids, Ionics 26 (2019) 2405–2412, https://doi.org/10.1007/s11581-019-03243-7.

[52] Y. Gao, N. Li, Y. Wu, W. Yang, S. Bo, Rethinking the design of ionic conductors using Meyer–Neldel–conductivity plot, Adv. Energy Mater. 11 (2021) 2100325, https://doi.org/10.1002/aenm.202100325.

[53] S. Lorger, R.E. Usiskin, J. Maier, Transport and charge carrier chemistry in lithium sulfide, Adv. Funct. Mater. 29 (2018) 1807688, https://doi.org/10.1002/adfm.201807688.

[54] N.F. Mott, Conduction in glasses containing transition metal ions, J. Non Cryst. Solids 1 (1968) 1–17, https://doi.org/10.1016/0022-3093(68)90002-1.

[55] V. Ambegaokar, B.I. Halperin, J.S. Langer, Hopping conductivity in disordered systems, Phys. Rev. B 4 (1971) 2612–2620, https://doi.org/10.1103/physrevb.4.2612.

[56] D. Yu, C. Wang, B.L. Wehrenberg, P. Guyot-Sionnest, Variable range hopping conduction in semiconductor nanocrystal solids, Phys. Rev. Lett. 92 (2024) 216802, https://doi.org/10.1103/physrevlett.92.216802.

[57] A. Ghosh, S. Bhattacharya, D.P. Bhattacharya, A. Ghosh, Hopping conduction in zinc vanadate semiconducting glasses, J. Appl. Phys. 103 (2008) 083703, https://doi.org/10.1063/1.2904933.

[58] M. Schnabel, A. Witzky, P. Löper, R. Gradmann, M. Künle, S. Janz, Electrical properties of recrystallised SiC films from PECVD precursors for silicon quantum dot solar cell applications, in: Proceedings of the 26th European Photovoltaic Solar Energy Conference and Exhibition, WIP-Renewable Energies, München, 2010, p. 454.

[59] B. Cai, M.L. Nakarmi, T.N. Oder, M. McMaster, N. Velpukonda, A. Smith, Elevated temperature dependent transport properties of phosphorus and arsenic doped zinc oxide thin films, J. Appl. Phys. 114 (2013) 223709, https://doi.org/10.1063/1.4845855.

[60] M.G. Moustafa, H.M.H. Saad, M.H. Ammar, Insight on the weak hopping conduction produced by titanium ions in the lead borate glassy system, Mater. Res. Bull. 140 (2021) 111323, https://doi.org/10.1016/j.materresbull.2021.111323.

[61] N.A. Wójcik, N.S. Tagiara, D. Möncke, E.I. Kamitsos, S. Ali, J. Ryl, R.J. Barczyński, Mechanism of hopping conduction in Be–Fe–Al–Te–O semiconducting glasses and glass–ceramics, J. Mater. Sci. 57 (2022) 1633–1647, https://doi.org/10.1007/s10853-021-06834-w.

[62] S. Demir, A. Tekin, Y.-T. Chan, C. Scheurer, K. Reuter, A.C. Luntz, J. Voss, Factors affecting the electron conductivity in single crystal $Li_7La_3Zr_2O_{12}$ and $Li_7P_3S_{11}$, ACS Appl. Energy Mater. 7 (2024) 2392–2404, https://doi.org/10.1021/acsaem.3c03092.

[63] S. Pacetti, C. Karlsson, E. Mijit, M. Drüschler, A. Di Cicco, N. Pinto, D. Bresser, J. Rezvani, Interplay of ionic and electronic properties of LPSCl with its micro- and macrostructural dynamics, J. Phys. Chem. C 130 (2026) 3040–3049, https://doi.org/10.1021/acs.jpcc.5c06227.

[64] D.O. Scanlon, A.B. Kehoe, G.W. Watson, M.O. Jones, W.I.F. David, D.J. Payne, R. G. Egdell, P.P. Edwards, A. Walsh, Nature of the band gap and origin of the conductivity of PbO_2 revealed by theory and experiment, Phys. Rev. Lett. 107 (2011) 246402, https://doi.org/10.1103/physrevlett.107.246402.

[65] X. Liu, R. Garcia-Mendez, A.R. Lupini, Y. Cheng, Z.D. Hood, F. Han, A. Sharafi, J. C. Idrobo, N.J. Dudney, C. Wang, C. Ma, J. Sakamoto, M. Chi, Local electronic structure variation resulting in Li "filament" formation within solid electrolytes, Nat. Mater. 20 (2021) 1485–1490, https://doi.org/10.1038/s41563-021-01019-x.

[66] H.-K. Tian, Z. Liu, Y. Ji, L.-Q. Chen, Y. Qi, Interfacial electronic properties dictate Li dendrite growth in solid electrolytes, Chem. Mater. 31 (2019) 7351–7359, https://doi.org/10.1021/acs.chemmater.9b01967.

[67] I. Riess, Four point Hebb-Wagner polarization method for determining the electronic conductivity in mixed ionic-electronic conductors, Solid State Ion. 51 (1992) 219–229, https://doi.org/10.1016/0167-2738(92)90204-3.